AGU PUBLICATIONS

JGR

Journal of Geophysical Research: Earth Surface

RESEARCH ARTICLE

10.1002/2016JF003999

Multidecadal climate and seasonal snow conditions in Svalbard

W. J. J. van Pelt[1,2], J. Kohler[2], G. E. Liston[3], J. O. Hagen[4], B. Luks[5], C. H. Reijmer[6], and V. A. Pohjola[1]

[1]Department of Earth Sciences, Uppsala University, Uppsala, Sweden, [2]Norwegian Polar Institute, Framcenter, Tromsø, Norway, [3]Cooperative Institute for Research in the Atmosphere, Colorado State University, Fort Collins, Colorado, USA, [4]Department of Geosciences, Oslo University, Oslo, Norway, [5]Institute of Geophysics, Polish Academy of Sciences, Warszawa, Poland, [6]Institute for Marine and Atmospheric Research Utrecht, Utrecht University, Utrecht, Netherlands

Key Points:
- SnowModel output generates a data set of climate and seasonal snow conditions in Svalbard for 1961-2012
- Spatial patterns and the multidecadal evolution of climate and snow parameters are analyzed and discussed

Correspondence to:
W. J. J. van Pelt,
ward.van.pelt@geo.uu.se

Citation:
Van Pelt, W. J. J., J. Kohler, G. E. Liston, J. O. Hagen, B. Luks, C. H. Reijmer, and V. A. Pohjola (2016), Multidecadal climate and seasonal snow conditions in Svalbard, *J. Geophys. Res. Earth Surf.*, *121*, 2100–2117, doi:10.1002/2016JF003999.

Received 23 JUN 2016
Accepted 12 OCT 2016
Accepted article online 18 OCT 2016
Published online 10 NOV 2016

Abstract Svalbard climate is undergoing amplified change with respect to the global mean. Changing climate conditions directly affect the evolution of the seasonal snowpack, through its impact on accumulation, melt, and moisture exchange. We analyze long-term trends and spatial patterns of seasonal snow conditions in Svalbard between 1961 and 2012. Downscaled regional climate model output is used to drive a snow modeling system (SnowModel), with coupled modules simulating the surface energy balance and snowpack evolution. The precipitation forcing is calibrated and validated against snow depth data on a set of glaciers around Svalbard. Climate trends reveal seasonally inhomogeneous warming and a weakly positive precipitation trend, with strongest changes in the north. In response to autumn warming the date of snow onset increased (2 days decade^{-1}), whereas in spring/summer opposing effects cause a nonsignificant trend in the snow disappearance date. Maximum snow water equivalent (SWE) in winter/spring shows a modest increase (+0.01 meters water equivalent (mwe) decade^{-1}), while the end-of-summer minimum snow area fraction declined strongly (from 48% to 36%). The equilibrium line altitude is highest in relatively dry inland regions, and time series show a clear positive trend (25 m decade^{-1}) as a result of summer warming. Finally, rain-on-snow in the core winter season, affecting ground ice formation and limiting access of grazing animals to food supplies, peaks during specific years (1994, 1996, 2000, and 2012) and is found to be concentrated in the lower lying coastal regions in southwestern Svalbard.

1. Introduction

In recent decades temperatures in the Arctic have increased at an amplified rate compared to the global mean [*Intergovernmental Panel on Climate Change*, 2013]. This "Arctic Amplification" is intimately linked to retreating sea ice cover and results from ice-atmosphere feedbacks, including the ice-albedo feedback [*Serreze et al.*, 2009] and the ice-infrared radiation feedback [*Bintanja and Van der Linden*, 2013]. Additionally, precipitation in the Arctic has increased in recent decades, in response to human-induced atmospheric moistening [*Zhang et al.*, 2012]. Trends in both precipitation and temperature in the Arctic are projected to increase during the remainder of the 21st century [*Serreze et al.*, 2009; *Bengtsson et al.*, 2011; *Bintanja and Selten*, 2014].

The focus of this study is on the Svalbard archipelago (Figure 1), situated at the northern end of the Atlantic warm water current and at the southern edge of wintertime sea ice. The climate in Svalbard is highly sensitive to variability and trends in sea ice cover [*Divine and Dick*, 2006; *Day et al.*, 2012] and atmospheric circulation patterns affecting the dominant wind direction [*Hanssen-Bauer and Førland*, 1998]. A strong seasonal contrast prevails in observed temperature trends with markedly more pronounced warming in winter/spring than in summer [*Førland et al.*, 2011; *Bintanja and Van der Linden*, 2013]. Observational precipitation records in Svalbard since the early and midtwentieth century reveal weakly positive trends, despite substantial local-scale and instrumental uncertainty [*Førland and Hanssen-Bauer*, 2000].

Changing temperature and precipitation conditions affect the evolution of the seasonal snowpack through its impact on accumulation, melt, and moisture exchange. Accumulation varies in space and time, with spatial variability being a product of local-scale (1–1000 m), regional-scale (1–100 km), and continental-scale (100–10000 km) processes. In a windy environment like Svalbard, local-scale accumulation variability is strongly governed by the interaction of topography and wind and associated processes of preferential precipitation and snow drift redistribution and sublimation [*Jaedicke and Gauer*, 2005; *Sauter et al.*, 2013; *Van Pelt et al.*, 2014]. At the regional and continental scale, accumulation variability is controlled by orographic lifting, distance to the moisture source, as well as movement and development of low-pressure systems

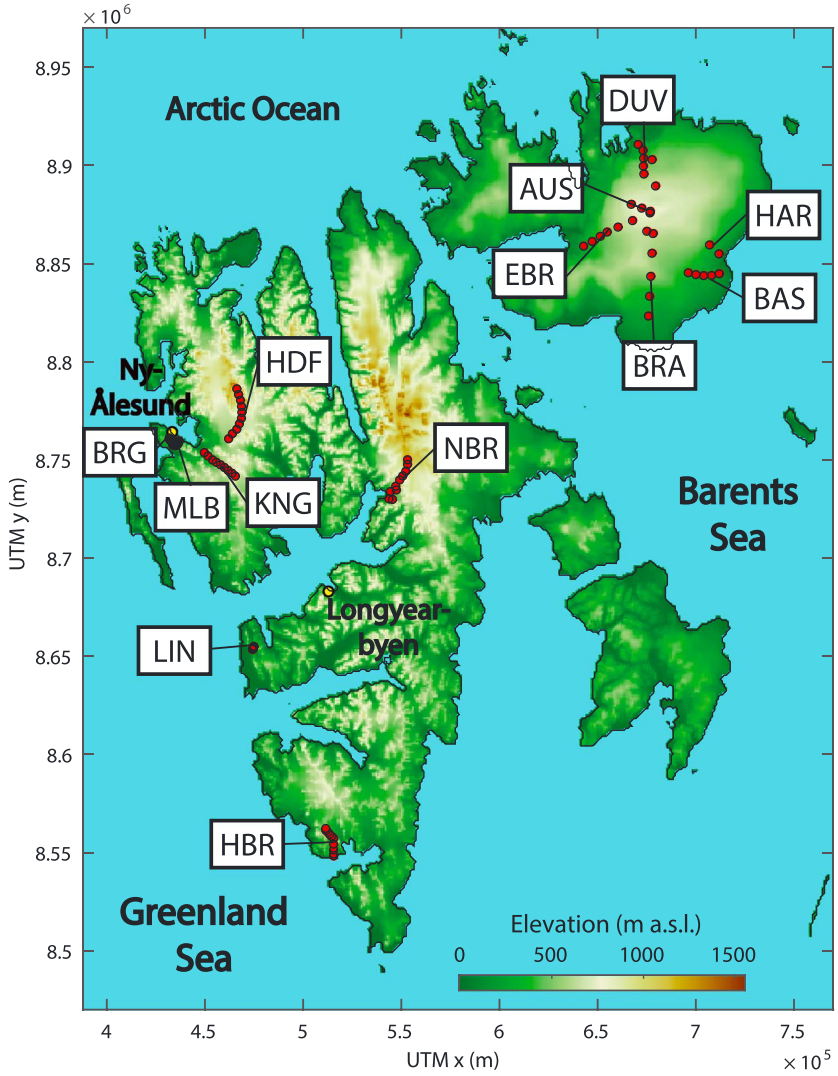

Figure 1. Topographic map of Svalbard. Red dots indicate the locations of collection of snow data, used for calibration of the precipitation downscaling (section 2.4). White labels mark the different glaciers used in the analysis [AUS = Austfonna (plateau), BAS = Basin-3, BRA = Bråsvellbreen, BRG = Austre Brøggerbreen, DUV = Duvebreen, EBR = Etonbreen, HAR = Hartogbukta, HBR = Hansbreen, HDF = Holtedahlfonna, KNG = Kongsvegen, LIN = Linnebreen, MLB = Midtre Lovénbreen, NBR = Nordenskiöldbreen]. Temperature measurements at coastal weather stations at Svalbard Airport (Longyearbyen) and Ny-Ålesund, and with an automatic weather station on Nordenskiöldbreen, were used for validation (section 3.1). The UTM coordinates used in this and following figures are within UTM zone 33X.

[*Taurisano et al.*, 2007; *Winther et al.*, 2003]. Moisture availability from the oceans around Svalbard is highly dependent on surface temperature and the presence or absence of seasonal sea ice around the archipelago [*Bintanja and Selten*, 2014].

Winter snowfall and riming control mass gain of the seasonal snowpack, while mass loss is determined by runoff of melt water and sublimation. Simulating surface mass and energy exchange requires detailed meteorological input to compute surface temperature, melt, and moisture transport. Coupling surface and snow processes is essential, since snowpacks exert a decisive influence on surface melt and runoff, in particular, through their impact on the surface albedo and their role in retaining melt water after refreezing. In some winters in Svalbard, excessive refreezing of rainfall leads to formation of a basal ice layer in the snowpack [*Kohler and Aanes*, 2004; *Hansen et al.*, 2011, 2014]. These "rain-on-snow" (ROS) events have been shown to pose a serious threat to Svalbard herbivores, since it limits their access to food supplies. In response to winter warming, the significance of ROS is expected to increase in a future climate [*Hansen et al.*, 2011].

Interannual variability and long-term seasonally inhomogeneous trends in temperature and precipitation affect both snow accumulation in autumn and winter as well as shrinkage in spring and summer, thereby affecting the duration of the snow-free season. The elevation above which snow survives summer melt is a proxy for the equilibrium line altitude (ELA), a term used to indicate the altitude at which annual mass gain and loss are in balance. For glaciers in Svalbard, covering 60% of the total land area, it has previously been shown that particularly for the large ice caps the surface mass balance is highly sensitive to small ELA changes due to their gently sloping geometry [*Möller and Schneider*, 2015; *Oerlemans and Van Pelt*, 2015]. At the same time, since the ELA is a product of interannual variability of both accumulation and ablation, it is also a useful composite measure to assess the climate sensitivity of seasonal snowpacks in a cold Arctic environment.

Extensive data of snow conditions in Svalbard have been collected in the most recent decades. Snow data come from a variety of sources, including meteorological stations, glacier mass balance stakes, ice core measurements, ground-penetrating radar profiles, satellite imagery, snow probing, and snow pit profiling [e.g., *Pohjola et al.*, 2002; *Hagen et al.*, 2003a; *Taurisano et al.*, 2007; *Möller et al.*, 2011; *Van Pelt et al.*, 2014]. In situ snow data have been highly valuable to study the local-scale distribution and development of snow conditions in Svalbard [e.g., *Winther et al.*, 2003; *Aas et al.*, 2016]. Additionally, the data provide an essential basis for calibration and validation for models simulating seasonal snow conditions. Since the availability of in situ snow data is limited in both space and time, the use of snow models is needed to better understand multidecadal trends and spatial patterns of seasonal snow conditions in Svalbard.

In this study, we present results from SnowModel, a seasonal snowpack modeling system connecting near-surface meteorological and snow processes [*Liston and Elder*, 2006a; *Liston and Hiemstra*, 2011], covering the period 1961–2012. To provide surface climate forcing to SnowModel, we used High Resolution Limited Area Model (HIRLAM) regional climate model output on an 11 km grid, downscaled onto the 1 km SnowModel grid. Stake winter balance measurements on a set of glaciers were used to optimize the downscaling of precipitation onto the grid. We first analyze the distributed multidecadal temperature and precipitation development. We then analyze trends and spatial variability of snow-related parameters, including minimum and maximum SWE, snow season length, perennial snow cover, ELA, and rain-on-snow. The model output comprises a relevant data set of multidecadal climate and snow conditions in Svalbard, with potential applications in terrestrial ecology, biology, hydrology, and glaciology.

2. Model and Setup

2.1. SnowModel

SnowModel is a snow evolution modeling system, developed for applications at scales ranging from the local to continental scale [*Liston and Elder*, 2006a]. SnowModel connects subroutines simulating the surface energy balance (EnBal), snow processes (SnowPack), and snow transport (SnowTran-3D) and can be applied in a variety of landscapes (both forested and nonforested) with different vegetation types.

The energy balance routine EnBal simulates energy exchange at snow surface in response to near-surface atmospheric conditions and evolving snow conditions [*Liston et al.*, 1999]. EnBal assumes a balance between absorbed solar radiation, incoming and outgoing longwave radiation, the sensible and latent turbulent heat flux, and the subsurface heat flux. The energy balance is solved for surface temperature, which cannot exceed the melting point; when it does, the excess energy is converted into melt. A snowpack model (SnowPack) simulates the evolution of seasonal snow depth, density, and temperature [*Liston and Sturm*, 1998; *Liston and Mernild*, 2012] in response to surface melt, moisture exchange, and precipitation. SnowPack accounts for densification processes of gravitational settling as well as internal refreezing of melt water. Finally, the SnowTran-3D module accounts for the interaction of terrain and wind to simulate wind-driven snow redistribution, a process that is typically relevant at horizontal scales ranging from 1 to 100 m.

Previous work with SnowModel has demonstrated its ability to simulate distributed snowpack evolution and runoff in complex terrain in a variety of geographical settings, including the USA, Arctic Canada, Siberia, the Alps, Tibet, Norway, Chile, Greenland, and Antarctica [e.g., *Mernild et al.*, 2010; *Liston and Hiemstra*, 2011]. A more complete overview of SnowModel applications is given in *Liston and Mernild* [2012].

2.2. Climate Input

While SnowModel can assimilate and extrapolate data from meteorological stations into the model domain, there are relatively few stations distributed around Svalbard; we use instead available output from a Regional Climate Model (RCM) to provide the required atmospheric forcing.

We use an existing data set of 3-hourly near-surface meteorological fields at 11 km resolution for Svalbard and its surroundings, generated with the High Resolution Limited Area Model (HIRLAM, version 6.4.2) [*Reistad et al.*, 2009]. HIRLAM is a hydrostatic numerical weather prediction model, which uses a semi-implicit semi-Lagrangian two-time level integration scheme for integration of the governing model equations [*Undén et al.*, 2002]. This enables dynamical downscaling and filtering of atmospheric fields. HIRLAM was forced at the boundaries with the European Centre for Medium-Range Weather Forecasts (ECMWF) ERA-40 and ERA-Interim reanalysis data fields [*Uppala et al.*, 2005; *Dee et al.*, 2011] of pressure, temperature, wind velocity, specific humidity, and cloud water in 40 vertical levels and further uses daily ECMWF fields of sea ice fraction, surface temperature, and snow depth. More details regarding the regional climate model setup and optimization can be found in *Reistad et al.* [2009, 2011]. We use 11 km near-surface (2–10 m) output of HIRLAM at 3 h resolution, provided by the Norwegian Meteorological Institute (met.no), and covering the period 1961–2012. HIRLAM output generated with a similar model setup and forcing has previously been used for hindcasting of winds and waves in the Norwegian and Barentsz Sea [*Reistad et al.*, 2011], as well as modeling of the glacier mass balance around Kongsfjorden in western Svalbard [*Van Pelt and Kohler*, 2015].

The 3-hourly fields from the HIRLAM RCM run were downscaled from the original 11 km grid onto the 1 km model grid using the meteorological distribution submodel MicroMet [*Liston and Elder*, 2006b]. MicroMet is an interpolation model, which uses known relations between meteorological variables and surface topography, elevation, and vegetation type, to generate the atmospheric input required by SnowModel at the desired spatial resolution [*Liston and Elder*, 2006b]. MicroMet projects temperature, relative humidity, precipitation, incoming shortwave and longwave radiation, air pressure, wind speed, and wind direction onto the 1 km model grid. Downscaling of temperature, relative humidity, precipitation, air pressure, and incoming longwave radiation is done using (seasonally dependent) elevation correction relations. Downscaling of wind speed and direction accounts for local topographic slope, curvature, and aspect relative to the wind direction. Downscaling of incoming shortwave radiation considers cloud cover, topographic slope, and aspect and distinguishes between direct and diffuse radiation. For more details regarding downscaling of the above parameters, the reader is referred to *Liston and Elder* [2006b]. For the precipitation downscaling, the elevation correction relation is calibrated against spring snow measurements, as discussed further in section 2.4. MicroMet distinguishes between precipitation falling as snow or rain by using a step transition at 2°C. This value is a standard value used in SnowModel, based on *Auer* [1974]. Alternatively, more recent estimates by *Dai* [2008] indicate a lower threshold temperature of 1.2°C. Uncertainty in the threshold temperature implies possible offsets in the modeled frequency and magnitude of rainfall; however, the impact on the discussed long-term rainfall trends is likely to be small.

2.3. Grid and Setup

We performed a 52 year simulation with SnowModel covering the period 1961–2012, to simulate the evolution of snow conditions in Svalbard, located in the high Arctic between 74–81°N and 10–35°E (Figure 1). The model grid dimensions are 550 by 468 km, with a total area of 257,400 km^2 and a land-covered area of 60,354 km^2. About 60% of the land area in Svalbard is covered by glaciers and ice caps with an estimated total volume of 6700–7000 km^3 [*Hagen et al.*, 2003b; *Martín-Español et al.*, 2015]. The topography of Svalbard is characterized by rugged terrain, with altitudes ranging from sea level to 1713 m above sea level (asl). The topographic map in Figure 1 is based on a 20 m resolution digital elevation model (DEM) constructed from aerial photographs of Svalbard covering the period 1961–2009 (DEM provided by the Norwegian Polar Institute, Tromsø, Norway: Terrengmodell Svalbard (S0 Terrengmodel), available at https://data.npolar.no/dataset/dce53a47-c726-4845-85c3-a65b46fe2fea). The DEM was averaged onto the 1 km resolution grid used for the SnowModel simulations. The climate and snow development are only simulated for land-covered grid cells.

The model was run from 1 September 1961 to 31 August 2012 at 3 h intervals, and output was stored as daily values. Wind-driven snow redistribution, as simulated by the submodel SnowTran-3D, would mainly affect the simulated snow distribution at scales smaller than the 1 km grid resolution and is therefore not taken into account. Additionally, routines specific to surface and snow processes in forested environments are not used, given the absence of vegetation higher than a few centimeters in Svalbard.

2.4. Calibrating Precipitation

An accurate description of seasonal snow development depends crucially on the precipitation input. As discussed in section 2.2, MicroMet interpolates HIRLAM precipitation onto the 1 km grid, adjusting for local topography using an elevation correction function. The optimum setup of the elevation correction function

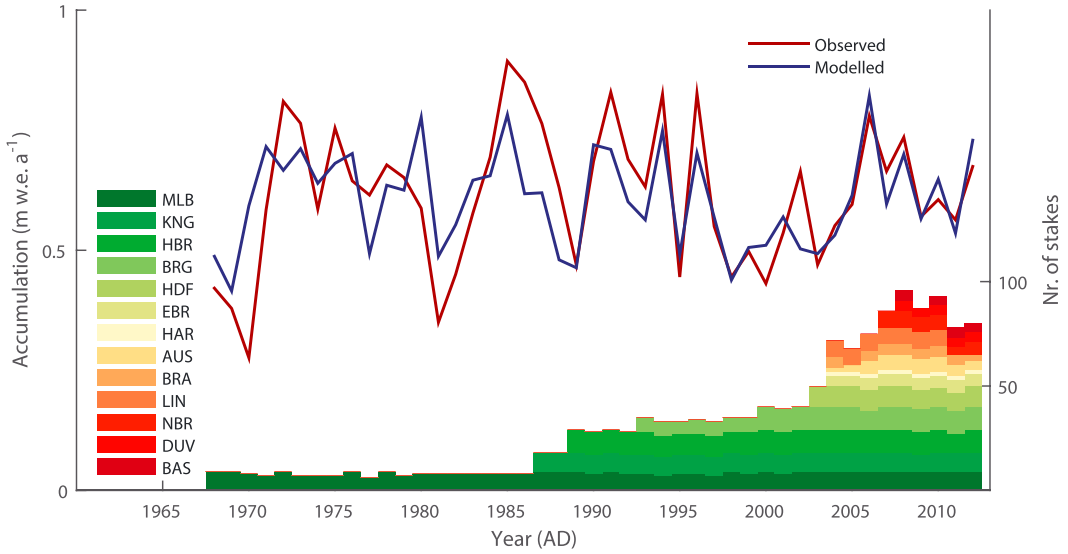

Figure 2. Time series comparison of modeled (blue) and observed (red) spring SWE, averaged for all available observation sites per year. The right axis shows the availability of SWE measurements from the different glaciers used for model calibration.

may vary between sites [*Liston and Elder*, 2006b], and calibration of the function against available data may therefore substantially improve model performance. To calibrate this elevation correction function for Svalbard, we use data from snow measurements in spring done annually at mass balance stake sites along centerlines of 13 glaciers (Figure 1).

Over the years a number of institutes have participated in collecting snow data on the different glaciers around Svalbard. Data sets used in the analyses presented herein include published and unpublished data from these institutes. Snow depth and density data have been collected by the Norwegian Polar Institute on glaciers in western Svalbard, including Kongsvegen, Holtedahlfonna, Midtre Lovénbreen, Austre Brøggerbreen, and Linnebreen [*Hagen et al.*, 1999; *Kohler et al.*, 2007; *Nuth et al.*, 2012; *Karner et al.*, 2013; *Van Pelt and Kohler*, 2015]. On Hansbreen, the Institute of Geophysics, Polish Academy of Sciences, has collected snow data since 1987 [*Grabiec et al.*, 2012]. On Austfonna, the University of Oslo and the Norwegian Polar Institute have recorded snow depths annually since 2004 [*Dunse et al.*, 2009; *Moholdt et al.*, 2010; *Østby et al.*, 2013; *Aas et al.*, 2016]. On Nordenskiöldbreen in central Svalbard snow data have been recorded by Uppsala University and Utrecht University since 2006 [*Van Pelt et al.*, 2012]. The time span of the observations for the different glacier records is shown in Figure 2, with the longest record from Midtre Lovénbreen going back to 1968. Snow depth has been estimated from mass balance stake readings, when done twice a year in autumn and spring, or by manual probing near the mass balance stake in case of yearly visits in spring. Along with the snow depth data, annual snow pit data on the individual glaciers were used to estimate bulk density, required to convert snow depth into SWE. The snow mass data provided observations of spring snow water equivalent on top of bare ice in the glacier's ablation area and on top of the previous year's summer surface in the accumulation zone. We estimate average snow mass measurement uncertainty at a few centimeter water equivalent, which presumably is much smaller than the local-scale (subgrid) variability inherent to point measurements. A total of 1442 individual SWE measurements were used in the analysis, with 892 measurements from northwest Svalbard (KNG, HDF, BRG, and MLB), 197 measurements in northeast Svalbard (BRA, EBR, HAR, AUS, DUV, and BAS), and 353 measurements in south-central Svalbard (LIN, HBR, and NBR).

In order to optimize agreement between modeled and observed SWE at stake sites in spring, we apply a linear elevation correction function to adjust precipitation for local topography:

$$P = P_0 \left[1 + \left(z - z_0\right) K\right] \quad , \tag{1}$$

where P is the adjusted precipitation, z is local elevation, and P_0 and z_0 are the model precipitation and elevation values interpolated using multipass Barnes interpolation [*Koch et al.*, 1983] from the 11 km HIRLAM

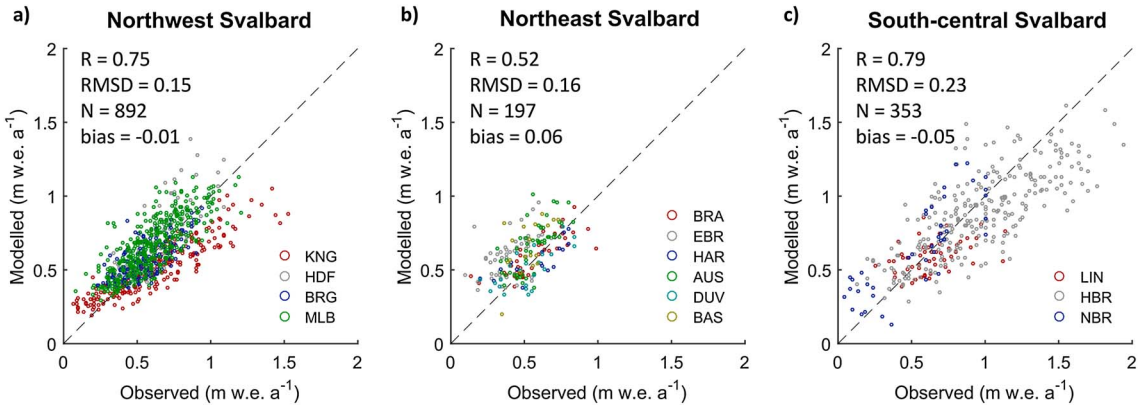

Figure 3. Modeled versus observed SWE on glaciers in (a) northwest, (b) northeast, and (c) south-central Svalbard. Indicated values of the RMSD and bias are in meters water equivalent (mwe).

output onto the 1 km grid. Model runs covering the stake observation period (1968–2012) were performed for a range of values of the coefficient K, representing the fractional precipitation-elevation gradient (in m^{-1}). Modeled SWE data were projected to the positions of the stake observations for all years by cubic interpolation. Snow measurements on Holtedahlfonna and Nordenskiöldbreen (up to 1123 and 1147 m asl) show that the precipitation lapse rate reduces to zero above an approximate elevation of around 1000 m asl [*Van Pelt et al.*, 2012; *Van Pelt and Kohler*, 2015]; accordingly, we cap the elevation correction (equation (1)) at that elevation. This implies that the precipitation distribution for grid cells with $z_0 > 1000$ m asl will be equal to the interpolated RCM precipitation distribution (P_0).

For all stake data, the best match between modeled and observed SWE was achieved for a precipitation lapse rate of 17.5% per 100 m elevation change ($K = 0.00175$ m^{-1}). A best value for K was estimated based on minimization of the root-mean-square deviation (RMSD) of modeled and observed precipitation for all SWE data. Modeled and observed SWE are compared in Figure 3. Highly significant R correlation coefficients ($P < 0.001$) of 0.75, 0.52, and 0.79 are found for northwest, northeast, and south-central Svalbard, respectively. The RMSD is within the range 0.15–0.23 mwe (meters water equivalent), equivalent to 25–30% of the mean observed precipitation for the three regions. Since we compare point observations of SWE with 1 km resolution model output, we argue that much of the remaining discrepancies between the modeled and observed SWE can be ascribed to this scale difference. Deposition of snow in Svalbard has previously been shown to vary substantially at scales smaller than the 1 km grid resolution, in particular, due to wind-driven snow transport and its dependence on local terrain exposure and orientation [*Pälli et al.*, 2002; *Van Pelt et al.*, 2014]. Mean biases between modeled and observed SWE are small (between −0.05 and 0.06 mwe a^{-1} for the three regions), which gives a mean bias of only −0.01 mwe a^{-1} for all the data. Altogether, the above demonstrates the model's ability to accurately simulate both the mean absolute precipitation and the regional precipitation variability.

Comparing modeled and observed accumulation shows there is good correlation after calibration for all SWE data ($R = 0.76$, i.e., more than half of the variance is explained) and the RMSD for all data points equals 0.17 mwe. After a model sensitivity run with $P = P_0$, i.e., with a zero fractional precipitation lapse rate ($K = 0$), the RMSD increases to 0.25 mwe as local-scale precipitation lapse rates are underestimated. On the other hand, doubling of K ($K = 0.0035$) causes the RMSD to increase to 0.23 mwe, which suggests an overestimation of local-scale precipitation lapse rates. The above demonstrates that selecting an optimized value for K while downscaling precipitation is an effective way to reduce uncertainty in simulated local-scale precipitation variability. A fixed value for K has been used for the entire grid and no tests have been done with spatially dependent values of K as there is insufficient data coverage to permit such a detailed parameterization. In addition to the applied linear elevation correction model, test runs with a nonlinear elevation correction model as in *Liston and Elder* [2006b], and with a constant absolute linear precipitation gradient (in mwe m^{-1}), have been performed and yielded weaker correlations.

A time series comparison of modeled and observed annual mean SWE, averaged for all the measurement sites during a year, shows that the model replicates well the temporal SWE variations (Figure 2). Agreement improves through time, as more data become available, suggesting that part of the offset can be ascribed to larger observational uncertainty due to limited data in the earlier part of the record.

3. Results and Discussion

In this section we present and discuss distributed output of the SnowModel run covering the period 1961–2012. We first discuss the climate development (section 3.1), before analyzing trends in seasonal snow conditions (section 3.2).

3.1. Climate Development (1961–2012)

Output of the HIRLAM climate model, forced with ECMWF reanalysis data, and downscaled onto a 1 km grid using MicroMet, provides a data set of near-surface climate variables for 1961–2012 at 3-hourly resolution. Here we analyze the spatial distribution and multidecadal trends in temperature and precipitation, which are the governing climate variables affecting the seasonal snowpack evolution.

3.1.1. Temperature

The 1961–2012 spatial pattern and development of 2 m temperature for Svalbard is illustrated in Figure 4. The long-term mean distribution of temperature on Svalbard (Figure 4a) is governed by both elevation lapse rates and a distinct negative lateral gradient from southwest to northeast Svalbard. The temperature distribution in Svalbard is intimately related to winter time sea ice, which commonly extends to the east and north of the archipelago; the southwest of Svalbard generally remains ice-free due to poleward heat transport through the West Spitsbergen Current [*Divine and Dick*, 2006]. Winter time sea ice acts as a platform for cold/dry air advection [*Day et al.*, 2012]; an effect which is most pronounced in northeastern Svalbard [*Isaksson et al.*, 2005].

A positive long-term trend in temperature is apparent for the whole of Svalbard (Figure 4b), with a mean trend of 0.8°C decade^{-1} ($p < 0.01$) and extrema ranging from 0.45°C decade^{-1} ($p < 0.01$) in the south to 1.3°C decade^{-1} ($p < 0.01$) in the north. Time series of seasonal temperatures reveal a clear seasonal inhomogeneity in the warming trend (Figure 4c). The trend in winter temperature (1.6°C decade^{-1}) is several times larger than in summer (0.2°C decade^{-1}). Yet both the summer (June-July-August) and winter (December-January-February) trends are statistically significant at a 99% confidence level ($p < 0.01$); the high significance of the weak summer trend can be ascribed to a low interannual variability (Figure 4c). The seasonal inhomogeneity in warming conforms with *Bintanja and Van der Linden* [2013], who concluded that recent and future Arctic winter warming exceeds summer warming by at least a factor 4.

We validate downscaled temperatures by comparing simulated time series to long-term meteorological observations at coastal weather stations at Ny-Ålesund since 1969 and Svalbard Airport since 1975 (data provided by the Norwegian Meteorological Institute; eKlima.no). To additionally validate modeled on-glacier temperatures, we also compare with temperature data observed with an automatic weather station at 520 m asl since 2009 on Nordenskiöldbreen in central Svalbard (Figure 1) [*Van Pelt et al.*, 2012]. A scatterplot comparison of modeled and observed daily mean temperatures for the three sites is shown in Figure 5. We find small mean temperature biases (simulated–observed) of −0.4°C, 0.3°C and −0.1°C for Ny-Ålesund, Svalbard Airport, and Nordenskiöldbreen, respectively. A high correlation coefficient of $R = 0.96$ ($p < 0.01$) for daily mean temperatures for all three sites confirms consistency of simulated and observed temperatures at daily and seasonal time scales. At longer time scales, the high correlation of annual mean temperatures $R = 0.81$ ($p < 0.01$) at Ny-Ålesund and $R = 0.85$ ($p < 0.01$) at Svalbard Airport indicates that the model captures most of the observed interannual variability in temperature. Additionally, long-term mean trends, averaged for both sites, agree well between the model (0.48°C decade^{-1}) and observations (0.53°C decade^{-1}).

3.1.2. Precipitation

Figure 6 shows the distribution, trend, and time series of precipitation on Svalbard between 1961 and 2012. The spatial distribution of precipitation (Figure 6a) is primarily governed by local topography, as is the case with temperature, and secondarily by a negative lateral gradient from southwest to northeast Svalbard. A visual comparison of the precipitation distribution in Figure 6a and similar maps presented by *Serreze et al.* [2015, Figure 1], based on output of the MERRA atmospheric reanalysis, *Lang et al.* [2015, Figure 7b], based on MAR regional climate model output, and *Aas et al.* [2016, Figure S1], based on output of the Weather Research and Forecasting (WRF) model, reveals reasonable agreement. Averaged over the grid, we find the mean precipitation lapse rate (below 1000 m asl) is 102 mmwe per 100 m elevation rise, which agrees well with a previous estimate of 97 mmwe per 100 m [*Winther et al.*, 2003]. Trends in Figure 6b reveal increasingly wet conditions in the north (maximum 0.05 mwe a^{-1} decade^{-1}, $p < 0.01$) and drier conditions in the south (minimum −0.03 mwe decade^{-1}, $p < 0.1$). Time series of land area-averaged annual precipitation show only a weak (nonsignificant) positive trend of 0.005 mwe a^{-1} decade^{-1} ($p > 0.1$). An indirect validation of the simulated precipitation trend comes from the time series comparison of simulated and observed spring SWE

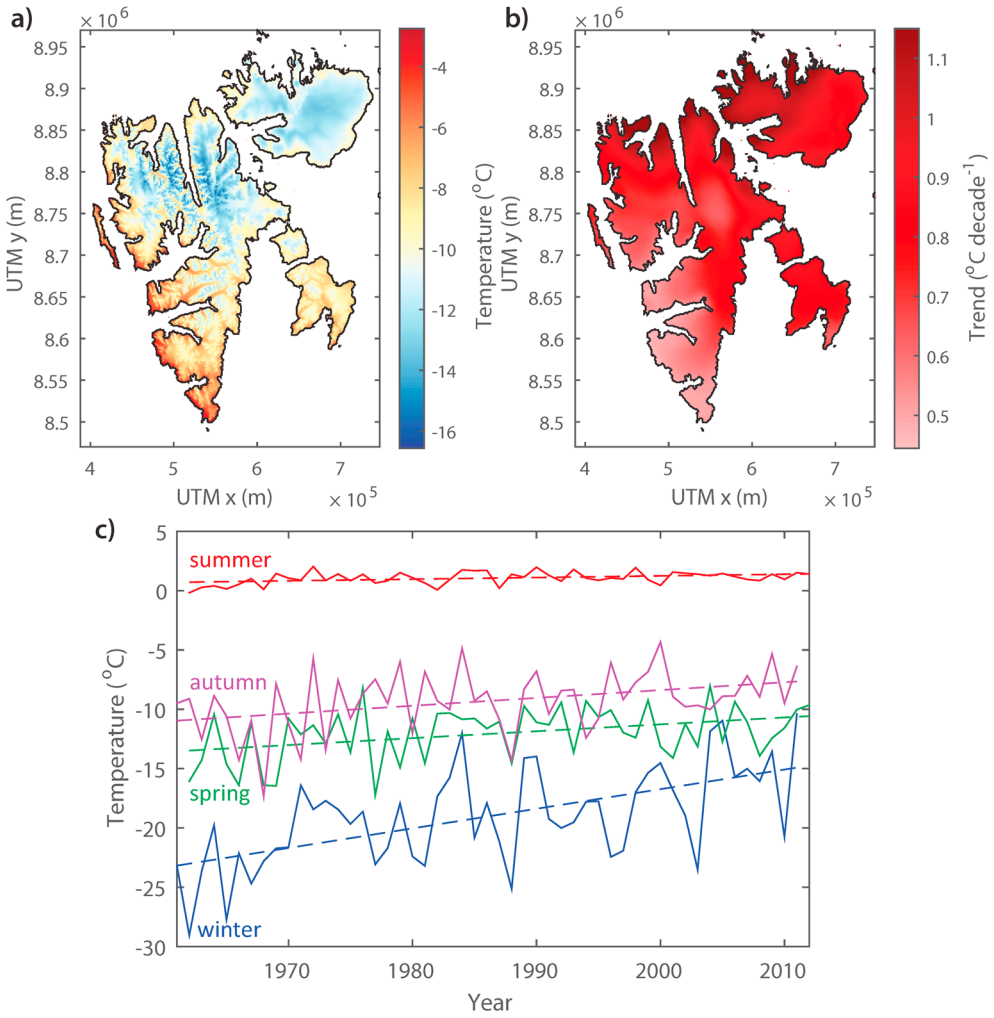

Figure 4. Temperature in Svalbard between 1961 and 2012: (a) long-term mean spatial distribution and (b) trend, and (c) land area-averaged seasonal temperature time series.

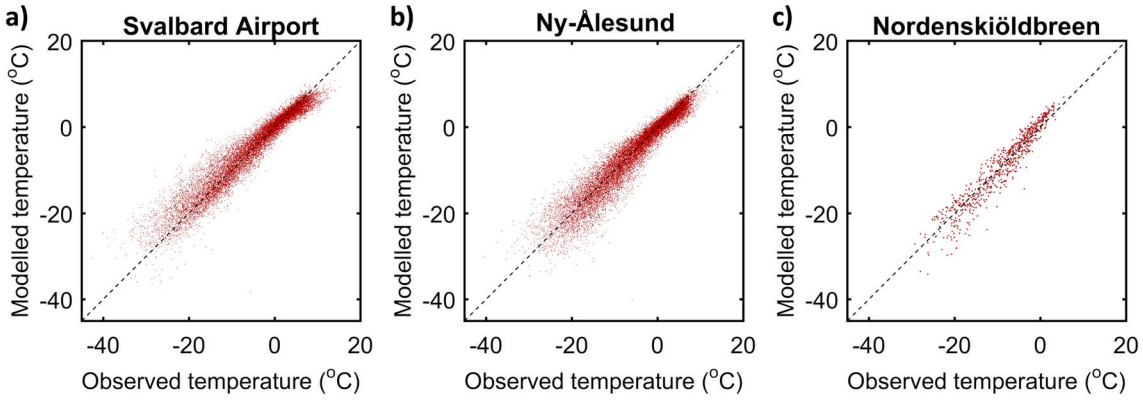

Figure 5. Comparison of modeled and observed daily mean temperatures at meteorological stations at (a) Svalbard Airport and (b) Ny-Ålesund, and at an automatic weather station on (c) Nordenskiöldbreen. Observational data from Svalbard Airport, Ny-Ålesund, and Nordenskiöldbreen cover the periods 1975–2012, 1969–2012, and 2009–2012, respectively.

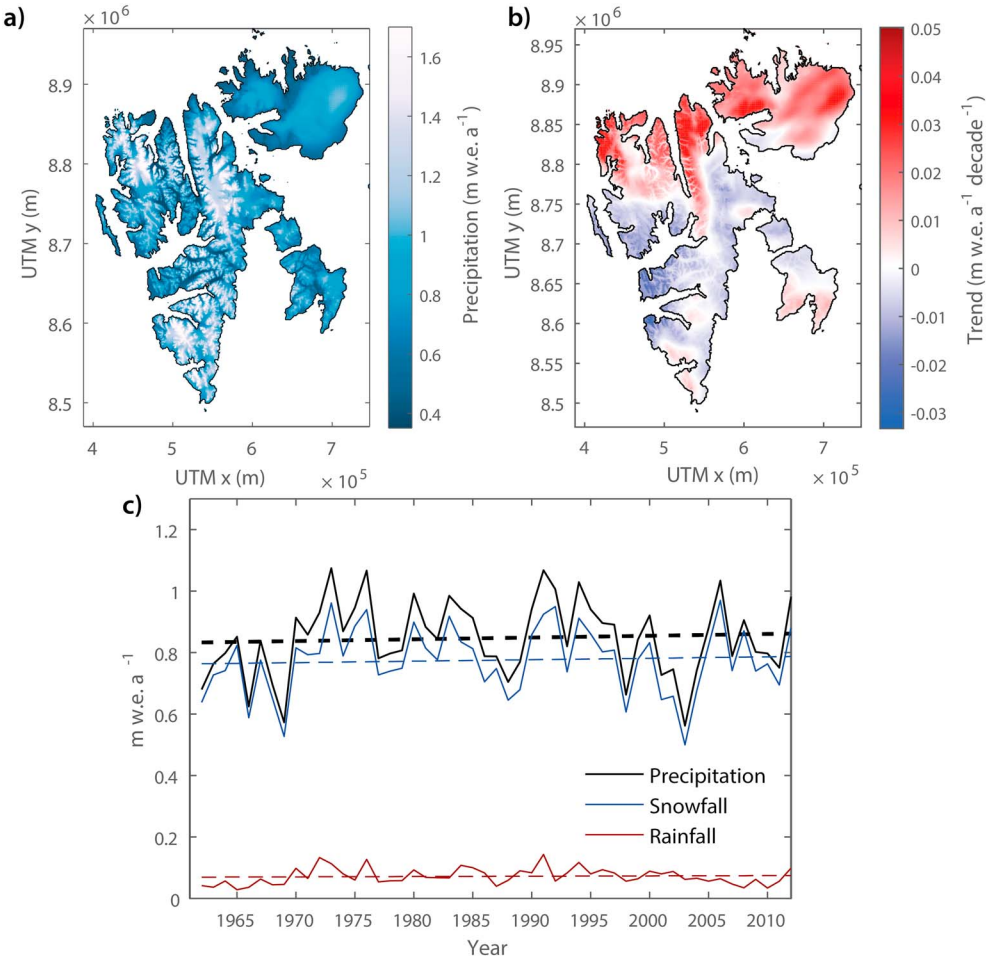

Figure 6. Precipitation in Svalbard between 1961 and 2012: (a) long-term mean spatial distribution and (b) trend, and (c) land area-averaged precipitation, snowfall, and rainfall time series with years defined between 1 September (preceding year) and 31 August.

(Figure 2), which reveals similar trends in modeled and observed time series. We do not directly compare modeled precipitation to observations, since the observational data from the coastal weather stations of Ny-Ålesund and Svalbard Airport are known to contain substantial biases, a result of the effect of wind on precipitation gauging. The associated precipitation undercatch is known to be substantial as well as temperature dependent, inducing false multidecadal trends in observed precipitation [*Førland and Hanssen-Bauer*, 2000].

Time series for both snowfall and rainfall are included in Figure 6c. As with total precipitation, there is a non-significant positive trend in snowfall (0.005 mwe a^{-1} decade^{-1}, $p > 0.1$). Despite substantial warming during the last decades, the land area-averaged rainfall trend is also found to be weak (0.001 mwe decade^{-1}, $p > 0.1$). This can be ascribed to a decrease in precipitation during the summer season (−0.009 mwe a^{-1} decade^{-1}, $p < 0.1$), which counterbalances the increased fraction of precipitation falling as rain. The 1961–2012 mean distribution of rainfall, shown in Figure 7a, shows most pronounced rain amounts in coastal regions in the southwest (up to 0.24 mwe a^{-1}), while rainfall is nearly absent in the northeast. The trend distribution (Figure 7b) illustrates a negative trend at low elevations (minimum −0.011 mwe a^{-1} decade^{-1}, $p < 0.1$), due to lower summer precipitation rates, and a substantial increase in rainfall at high elevations (maximum 0.012 mwe a^{-1} decade^{-1}, $p < 0.1$), due to higher temperatures.

3.2. Seasonal Snow Trends (1961–2012)

The discussed climate variability and trends affect the evolution of seasonal snow. In this section, we analyze the 1961–2012 development of seasonal snow parameters, including the dates of snow onset and disappearance, minimum and maximum SWE, rain-on-snow amounts, perennial snow cover, and the equilibrium line altitude (ELA).

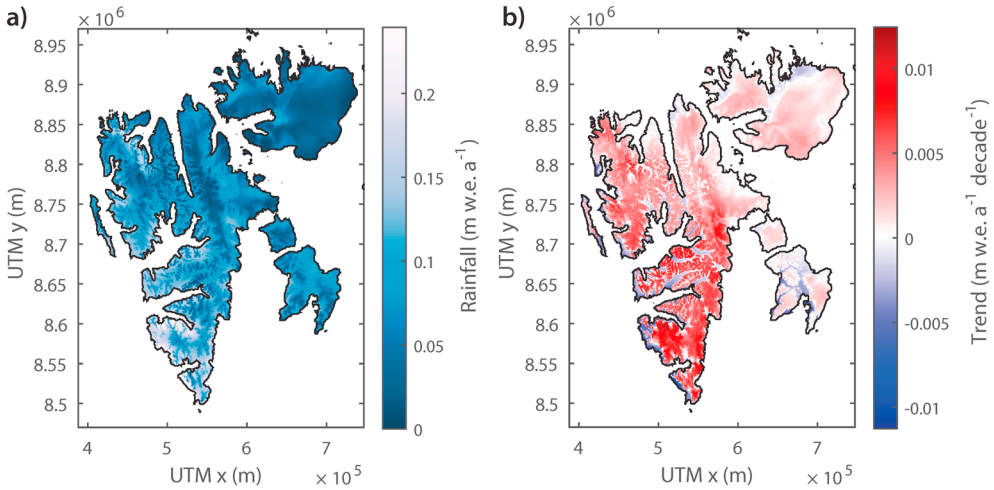

Figure 7. Rainfall in Svalbard between 1961 and 2012: (a) long-term mean spatial distribution and (b) trend.

3.2.1. Snow Season Duration

In autumn, the day of year (DOY) when the snowpack starts to form is determined by precipitation type and amount as well as late-season melt. We define the snow onset date at a certain grid point as the day of the year after which the surface is uninterruptedly covered by snow. The distribution of the snow onset date (Figure 8a) shows a strong temperature dependence, with earlier onset of snowpack development at high elevations and toward the northeast of Svalbard. White areas (Figure 8b) indicate that the onset date could not be defined as seasonal snow accumulation survived summer melt in at least half of the years in the simulation period. There is a consistent positive trend in the snow onset date; i.e., snow forms later in the year, for the whole of Svalbard, by up to a maximum of 5 d decade^{-1} ($p < 0.01$). Time series in Figure 8e reveal an average snow onset date at DOY 248 (5 September) and a mean trend of 1.8 d decade^{-1} ($p < 0.1$).

In spring, the DOY on which the snowpack vanishes is controlled by melt rates and the winter snow accumulation. In low-precipitation and high-temperature areas, i.e., in the low-lying valleys in central Svalbard, snow vanishes earliest in the season, on average in the beginning of June (Figure 8c). There is a general trend (Figure 8d) of earlier snow disappearance in central Svalbard (minimum −1 d decade^{-1}, $p < 0.1$) and later disappearance in the east and north of Svalbard (maximum 4 d decade^{-1}, $p < 0.01$). This pattern is similar to the precipitation trend (Figure 6b), implying that trends in snow disappearance are to a larger extent controlled by trends in winter snowfall rather than trends in spring and summer melt. As a result, even with the strong spring and summer warming trends (Figure 4c), the positive trend for the snow disappearance date (0.7 d decade^{-1}) is not significant ($p > 0.1$).

With positive trends for both the snow disappearance and onset dates, and with the latter trend being more pronounced, the snow-free season length increased slightly, by 1.2 d decade^{-1} ($p < 0.1$).

3.2.2. Minimum and Maximum SWE

Figure 9 shows the distribution, trends, and time series of mean end-of-summer minimum and spring maximum SWE. Since maximum SWE (Figure 9a) is by definition equivalent to cumulative accumulation since the date of snow onset in autumn, the trend and land area-averaged time series of the maximum SWE (Figures 9b and 9e) show strong similarity to those for precipitation (Figures 6b and 6c). We find a mean maximum SWE of 0.68 mwe, with a weak mean trend of 0.01 mwe decade^{-1} ($p > 0.1$). Trends in Figure 9b range between −0.03 mwe decade^{-1} ($p > 0.1$) in the west and 0.05 mwe decade^{-1} ($p < 0.1$) in the north.

The 1961–2012 mean minimum SWE (Figure 9c) ranges between 0 at low elevations (implying no years with end-of-summer snow) and 0.85 mwe at high elevations in the northwest of Svalbard. Trends in Figure 9d range between −0.07 mwe decade^{-1} ($p < 0.01$) in the southwest and 0.03 mwe decade^{-1} in the north ($p < 0.01$) giving a weak land area-averaged trend of −0.01 mwe decade^{-1} ($p > 0.1$).

3.2.3. Perennial Snow Cover and ELA

Based on annual minimum snow cover maps, we calculated the perennial snow fraction, defined as the fraction of the total number of simulated years that seasonal snow did not fully melt in summer. For a certain location, a perennial snow fraction of zero means that snow melts away every summer, while a value of 1

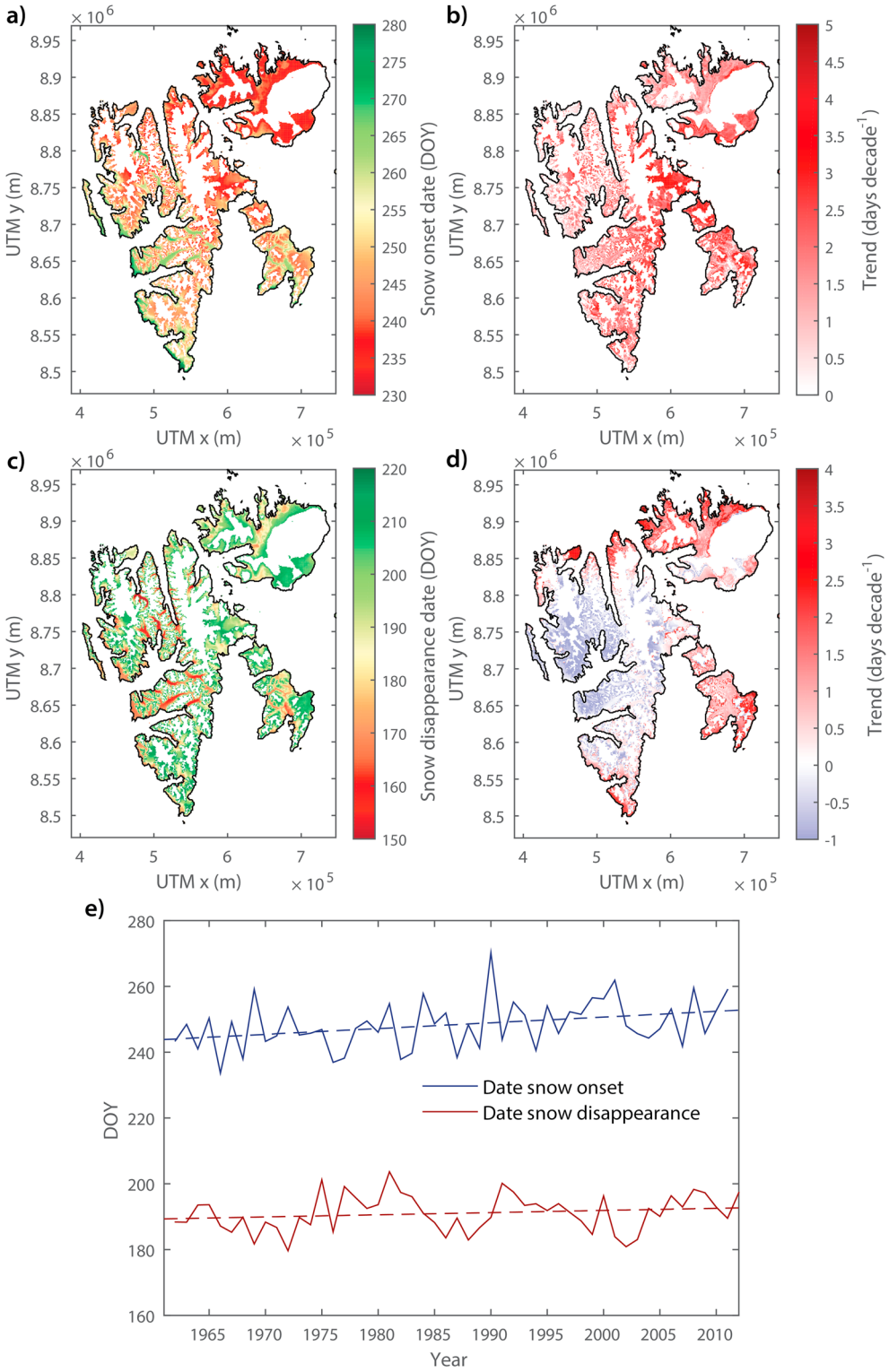

Figure 8. Snow onset and disappearance dates in Svalbard between 1961 and 2012: (a, c) long-term mean spatial distribution, (b, d) distributed trends, and (e) land area-averaged time series.

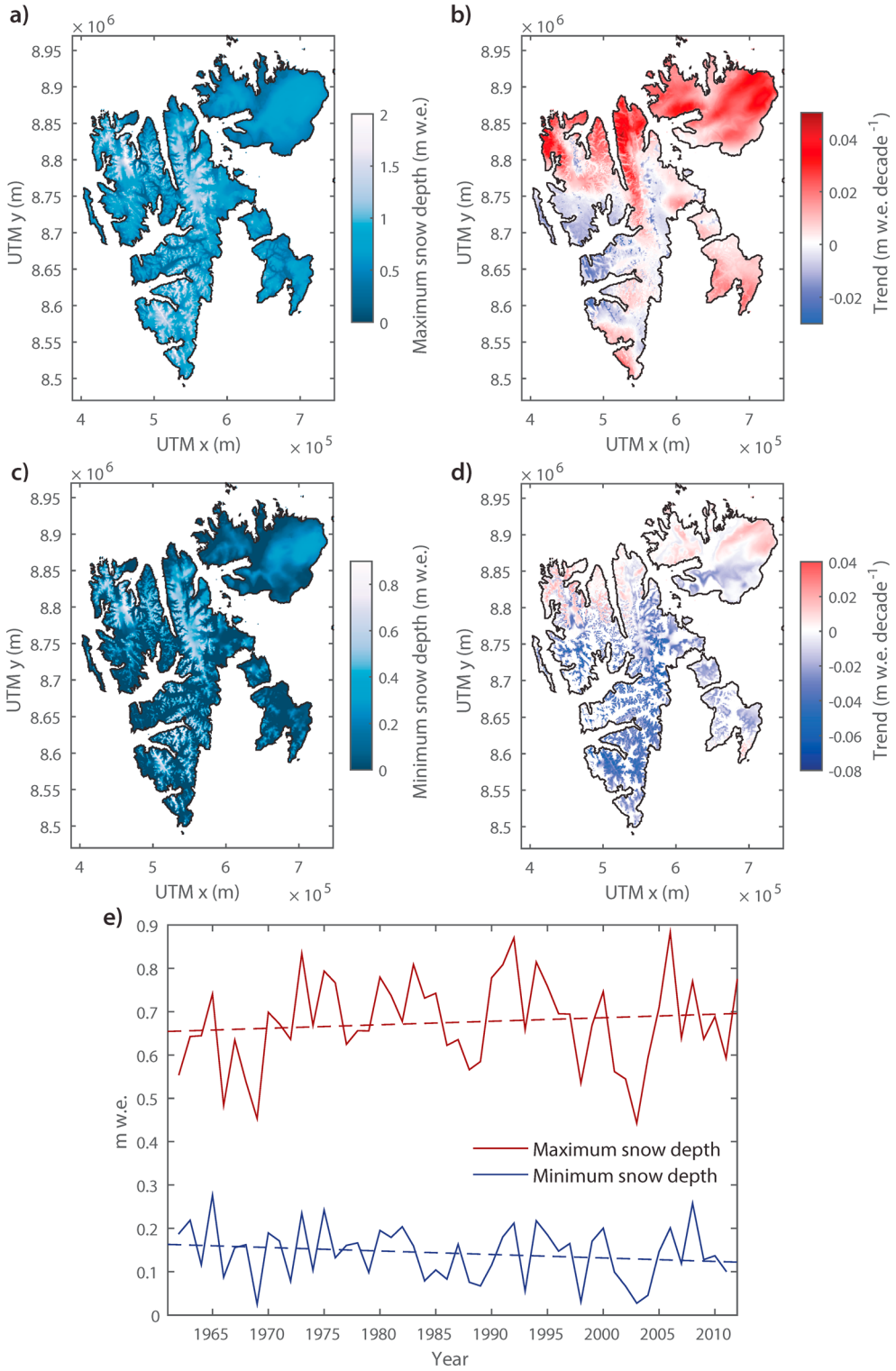

Figure 9. Seasonal maximum and minimum SWE in Svalbard between 1961 and 2012: (a, c) long-term mean spatial distribution, (b, d) distributed trends, and (e) land area-averaged time series.

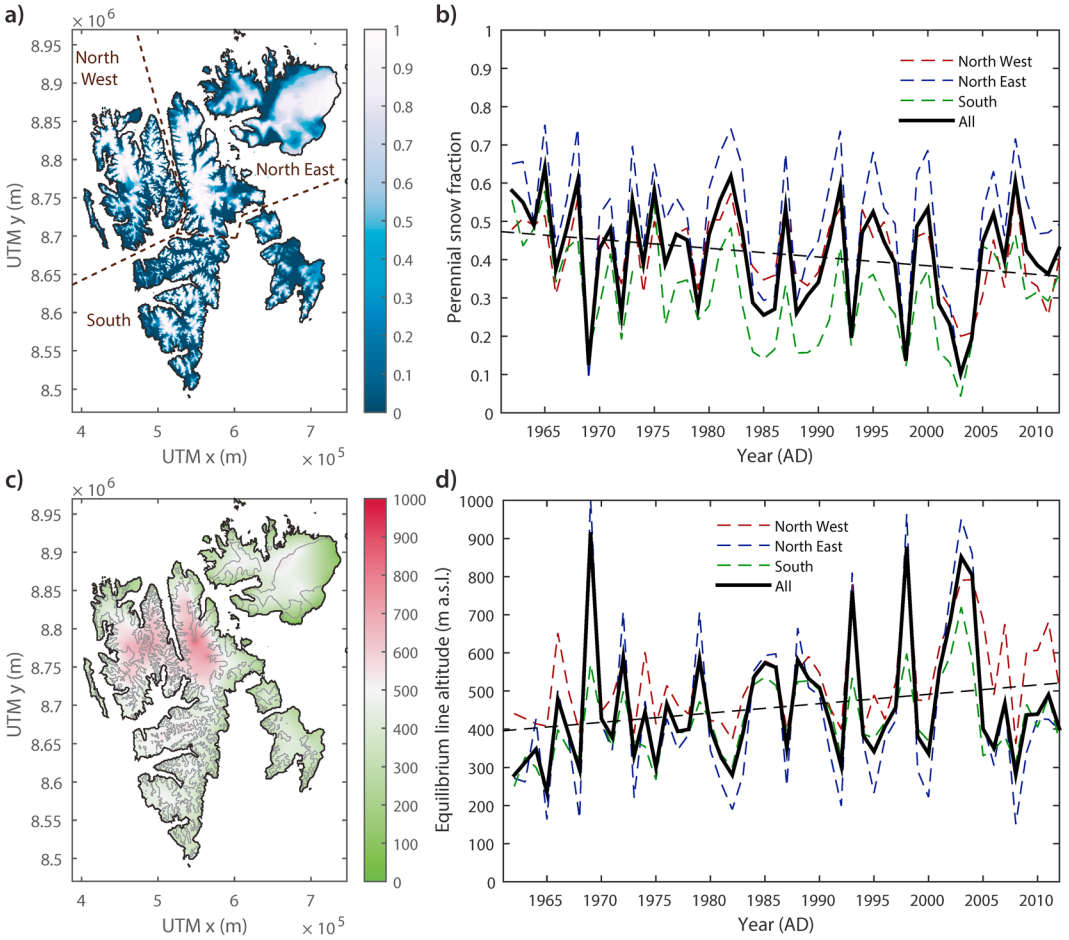

Figure 10. Perennial snow fraction and equilibrium line altitude in Svalbard between 1961 and 2012: (a, c) long-term mean spatial distribution, and (b, d) land area-averaged time series with years defined between 1 September (preceding year) and 31 August. Dashed colored lines in Figures 10b and 10d represent time series of spatial mean values for the regions indicated in Figure 10a. Gray lines in Figure 10c represent the 50% perennial snow fraction contour.

implies that some seasonal snow remains at the end of summer during all simulated years. The perennial snow fraction, shown in Figure 10a, is a clear function of elevation. The altitude at which the perennial snow fraction equals 0.5, i.e., snow melts away in summer during half of the simulated years, marks the elevational transition from seasonal to perennial snow. On glaciers, this line approximates the transition from ablation area (negative mass balance) to accumulation area (positive mass balance) and the 50% perennial snow fraction elevation can hence be regarded as an indicator of the equilibrium line altitude (ELA). The 1961–2012 perennial snow cover map (Figure 10a) shows a large portion of the domain with a perennial snow fraction greater than zero. There is also substantial interannual variability in perennial snow fraction (Figure 10b); whether averaged over the entire archipelago or subregions, the perennial snow fraction ranges from 10 to 70%, with a negative trend of −2.3% decade^{-1} ($p < 0.1$).

An ELA map was constructed by interpolating and extrapolating elevations for which the perennial snow fraction equals 50% (Figure 10c). Gray lines mark the 50% perennial snow fraction contour line, representing the locations where the ELA is actually known; for the remainder of the grid the ELA was estimated by interpolation and extrapolation using the MATLAB routine `inpaint_nans` (D'Errico, 2012; https://www.mathworks.com/matlabcentral/fileexchange/4551-inpaint-nans). Long-term mean ELA values range from sea level in the northeast to 900 m asl in central Svalbard. The lowest values are found in coastal regions and highest values on the high ice plateaus in central and northwestern Svalbard. Time series of the ELA show strong interannual variability with values ranging between 200 and >900 m asl (Figure 10d). A comparison of the ELA time series for 2000–2010 with time series presented in *Möller et al.* [2016, Figure 7e] reveals close resemblance. For the period 1961–2012 we find a mean ELA for Svalbard of 459 m asl, with a positive trend of

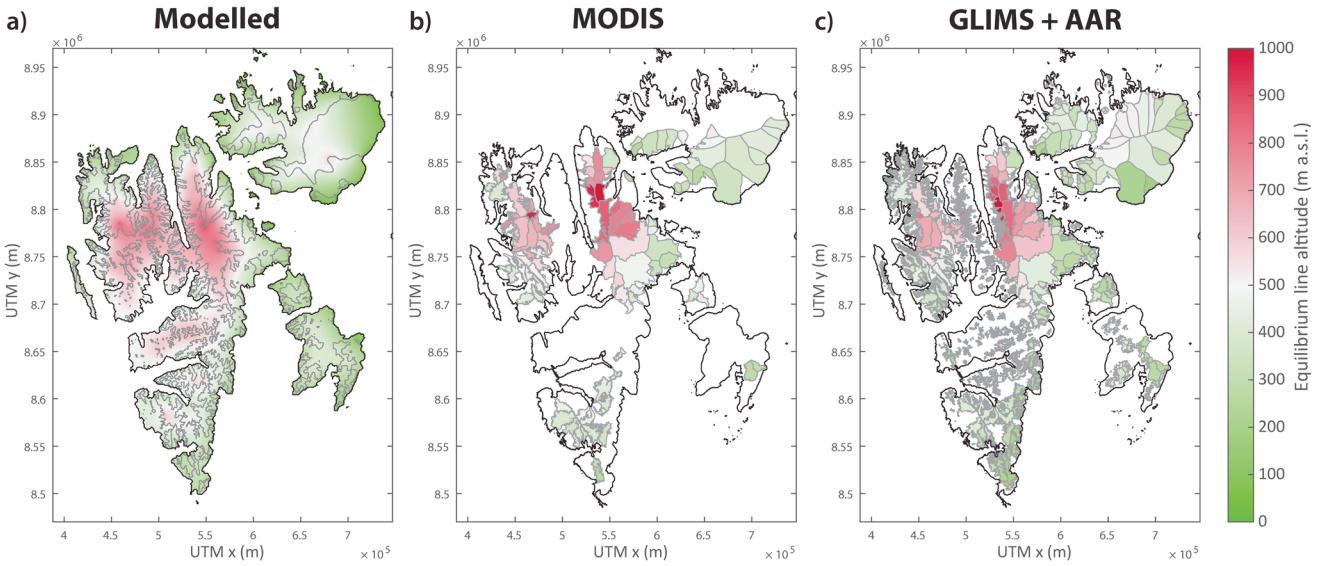

Figure 11. Comparison of the simulated 2000–2012 (a) mean ELA, (b) MODIS-derived ELA, and (c) AAR-based ELA.

25 m decade^{-1} ($p < 0.1$). The land area-averaged time series (Figure 10d) correlates strongly with summer temperature ($R = 0.69$, Figure 4c) and anticorrelates strongly with maximum spring SWE ($R = -0.57$; Figure 9e), with both correlations significant at a 99% confidence level ($p < 0.01$). This indicates that the ELA is a product of both summer melt and winter accumulation. Given the higher significance of the summer temperature trend compared to the maximum SWE trend, we find that the positive ELA trend (Figure 10d) can be attributed mostly to increased summer temperature. Comparing ELA time series for different regions in Svalbard, we find that temporal ELA variability is much smaller in the south than in the north; a similar discrepancy was found by *Möller et al.* [2016]. This can be ascribed to a generally steeper precipitation lapse rate in southern Svalbard, compared to the north, which reduces the ELA sensitivity to interannual precipitation and temperature variations.

We validated the simulated ELA distribution for the period 2000–2012 through a comparison with two independent ELA estimates based on (1) satellite-derived snowline data (MODIS) and (2) elevations from a glacier hypsometry database (GLIMS) assuming a fixed accumulation area ratio (AAR).

We used MODIS (Moderate Resolution Imaging Spectroradiometer) satellite data, specifically the MCD43A3 albedo product, to track the snowline over the course of each summer in the period 2000–2012, on a set of 104 glaciers in Svalbard (J. Kohler, unpublished data, 2015). Snowline estimates were obtained from the albedo contrast between winter snow and the underlying ice or firn. It was assumed that the mean elevation of the maximum snowline in each summer was a good proxy for the ELA. While the true ELA is at a lower elevation than the detected snowline, due to the formation of superimposed ice [*König et al.*, 2002], in practice, this amounts to only a small elevational difference. Using an automated detection algorithm (J. Kohler, unpublished data, 2015), MODIS-based ELA proxy values were determined for 104 glaciers in Svalbard of 50 km^2 or larger (Figure 11b).

The second validation method used glacier outlines and hypsometries from the GLIMS (Global Land Ice Measurements from Space) database to derive ELA estimates for 1583 glacier outlines in Svalbard [*König et al.*, 2014]. By assuming a fixed accumulation area ratio (AAR) of 0.60, the ELA was extracted directly from the hypsometry. The AAR value used is based on estimates on Vestfonna (NE Svalbard) of 0.59 for 2006–2015 [*Möller and Schneider*, 2015] and 0.60 on Austfonna for 2003–2008 [*Moholdt et al.*, 2010]. The resulting ELA distribution is shown in Figure 11c.

We compared the modeled ELA distribution (Figure 11a) to the independent MODIS-based (Figure 11b) and AAR-based (Figure 11c) distributions. To facilitate comparison, modeled values in Figure 11a were averaged per glacier basin. Overall, the patterns are similar. As suggested in *Hagen et al.* [2003a], spatial variability in the ELA is determined mainly by precipitation variability, with lower ELA in wet coastal regions and higher ELA farther inland at greater distance to the moisture source. Comparing modeled and MODIS-based ELA

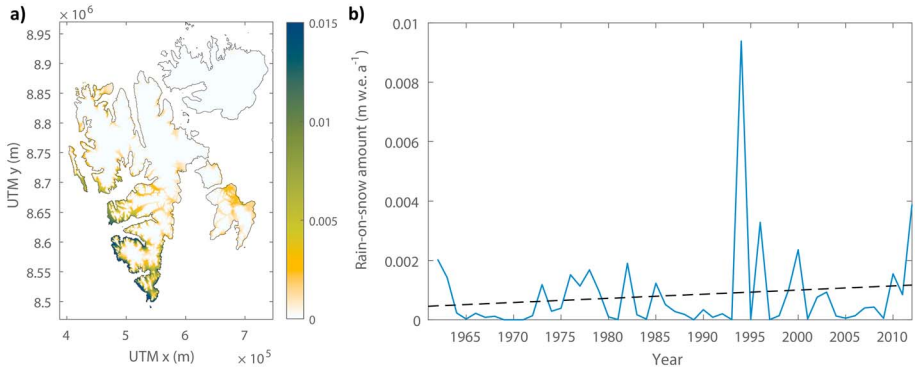

Figure 12. Rain-on-snow amount in Svalbard between 1961 and 2012: (a) long-term mean spatial distribution and (b) land area-averaged time series. Rain-on-snow is calculated between November (preceding year) and March.

reveals a mean bias of only 3 m, standard deviation of 130 m asl, and a correlation for all shared glacier basins ($N = 99$) of $R = 0.69$ ($p < 0.01$). Comparing modeled and AAR-based ELA gives a mean bias of 24 m, standard deviation of 93 m asl, and a correlation for all shared glaciers ($N = 478$) of $R = 0.80$ ($p < 0.01$). Based on the above, we conclude that the model is able to simulate well the mean absolute ELA as well as its spatial distribution. Since the ELA is collectively determined by snow accumulation and melt water runoff, the above ELA comparison provides an important indirect validation of simulated snow melt. A more detailed validation of distributed snow melt and dates of snow onset and disappearance is currently infeasible, given a lack of observational data.

3.2.4. Rain-on-Snow

While melt rates during the core winter season (November–March) in Svalbard are negligible, substantial amounts of rainwater can percolate into the winter snowpack during major winter warm events. Refreezing of percolating water in cold winter snow causes densification and, in case of substantial rain amounts, the formation of a basal ice layer at the base of the snowpack. Basal ice layers are known to substantially impact the growth rate of herbivores in Svalbard, as it limits accessibility of food supplies [e.g., *Kohler and Aanes*, 2004; *Hansen et al.*, 2011, 2014]. We defined the annual rain-on-snow (ROS) amount as the sum of rainfall between November (preceding year) and March. The distribution of ROS amount (Figure 12a) shows its primary significance in coastal regions in the southwest of Svalbard and negligible ROS amounts at higher elevations. ROS is highly variable from year to year (Figure 12b), with maxima in 1994, 1996, 2000, and 2012. The maxima in 1994, 1996, and 2012 coincide with years with extreme winter rainfall events, as shown in *Serreze et al.* [2015, Table 3]. Similar to *Serreze et al.* [2015], we find a nonsignificant trend of ROS amount (0.0001 mwe decade^{-1}, $p > 0.1$), despite the substantial winter warming over the simulation period. The low significance of the ROS trend can, to a large extent, be ascribed to the scarcity of ROS events.

4. Conclusions

A simulation of multidecadal seasonal snow conditions in Svalbard was done with the snowpack evolution model SnowModel. Climate fields were generated by the regional climate model HIRLAM and downscaled onto the 1 km model grid using the submodel MicroMet. Downscaled precipitation was calibrated against annual snow measurements on 13 glaciers in Svalbard, thereby minimizing uncertainty in simulated snow accumulation. From the model output, we discussed variability and trends of climate and seasonal snow conditions in Svalbard for the period 1961–2012.

Climate trends over the simulation period reveal seasonally inhomogeneous warming, with strongest trends in the north of Svalbard. Precipitation trends show increasingly wet conditions in the north and slightly drier conditions in central and southern Svalbard; averaged across the entire archipelago, only a weak positive trend is found. Summer warming caused increased rainfall at high elevations, offsetting a weak decline in summer precipitation. Rain-on-snow is found to be substantial at low elevations in the west and southwest of Svalbard, and shows clear maxima in specific years (1994, 1996, 2000, and 2012). The sporadic nature of ROS events contributes to strong interannual variability, and hence, the long-term trend is found to be nonsignificant.

In response to autumn warming the date of snow onset has increased, whereas in spring/summer opposing effects of earlier melt onset and higher winter accumulation caused a nonsignificant trend in the date of snow disappearance. Maximum SWE is largely controlled by winter accumulation, implying a weak positive land area-averaged trend and significant spring snowpack thickening in the north. The perennial snow fraction is governed by both winter accumulation and summer melt and shows a significant negative trend (-0.02 decade^{-1}). The ELA distribution, derived from the 50% perennial snow fraction contour, shows low values in coastal regions and higher values farther inland in response to precipitation variability. Summer warming has caused the ELA to rise by 25 m decade^{-1} over the simulation period. Comparison of the simulated ELA distribution- and observation-based maps from MODIS snow cover data and the GLIMS database shows good agreement and indirectly serves as a validation of simulated spatial distributions of snow accumulation and melt.

This continuous, high-resolution data set of climate and snow parameters for Svalbard is not only of use for detecting multidecadal spatiotemporal variability and trends, it may also serve as input in a wide range of applications, ranging from runoff modeling to ground ice studies to ecosystem studies. For smaller domains in Svalbard, SnowModel can potentially be applied to simulate the snow distribution evolution with higher spatial resolution. At spatial scales smaller than 1 km, it becomes desirable to account for local-scale variability caused by wind-driven snow transport and sublimation, which is incorporated in SnowModel's subroutine SnowTran-3D [*Liston and Sturm*, 1998; *Liston et al.*, 2007].

Acknowledgments

This work was carried out within SVALI, funded by the Nordic Top-level Research Initiative (TRI), and is SVALI publication 77. For all the published data used in this study, references are cited; unpublished data are described and shown and the groups involved in data collection are indicated. We are grateful to the Norwegian Meteorological Institute for providing the HIRLAM regional climate model output and for providing access to the meteorological station data for Ny-Ålesund and Svalbard Airport through the eKlima data portal (http://eklima.met.no). This work further relies on snow data for calibration of precipitation. Many have contributed over the years to the snow measurements obtained in connection with glacier mass balance measurements, too many to thank in one place. The Norwegian Polar Institute (J. Kohler) has provided access to the snow measurements from Kongsvegen, Holtedahlfonna, Midtre Lovénbreen, Austre Brøggerbreen, and Linnebreen. Snow data for Austfonna were provided by the University of Oslo (J.O. Hagen) and the Norwegian Polar Institute (J. Kohler). The Institute of Geophysics of the Polish Academy of Sciences (B. Luks) has given access to the snow data for Hansbreen. Finally, the snow data and the AWS temperature data from Nordenskiöldbreen are provided by Uppsala University (V. Pohjola and W. van Pelt) and Utrecht University (C. Reijmer). Veijo Pohjola acknowledges a grant from the Swedish Science Council for logistical support during fieldwork. All the data used in this study can be accessed by contacting the above contact persons or the related institutes.

References

Aas, K. S., T. Dunse, E. Collier, T. V. Schuler, T. K. Berntsen, J. Kohler, and B. Luks (2016), The climatic mass balance of Svalbard glaciers: A 10-year simulation with a coupled atmosphere-glacier mass balance model, *Cryosphere*, *10*(3), 1089–1104, doi:10.5194/tc-10-1089-2016.

Auer, A. H. (1974), The rain versus snow threshold temperatures, *Weatherwise*, *27*(2), 67–67, doi:10.1080/00431672.1974.9931684.

Bengtsson, L., K. I. Hodges, S. Koumoutsaris, M. Zahn, and N. Keenlyside (2011), The changing atmospheric water cycle in Polar Regions in a warmer climate, *Tellus A*, *63A*(5), 907–920, doi:10.1111/j.1600-0870.2011.00534.x.

Bintanja, R., and F. M. Selten (2014), Future increases in Arctic precipitation linked to local evaporation and sea-ice retreat, *Nature*, *509*(7501), 479–482, doi:10.1038/nature13259.

Bintanja, R., and E. C. Van der Linden (2013), The changing seasonal climate in the Arctic, *Sci. Rep.*, *3*, 1–8, doi:10.1038/srep01556.

Dai, A. (2008), Temperature and pressure dependence of the rain-snow phase transition over land and ocean, *Geophys. Res. Lett.*, *35*, L12802, doi:10.1029/2008GL033295.

Day, J. J., J. L. Bamber, P. J. Valdes, and J. Kohler (2012), The impact of a seasonally ice free Arctic Ocean on the temperature, precipitation and surface mass balance of Svalbard, *Cryosphere*, *6*(1), 35–50, doi:10.5194/tc-6-35-2012.

Dee, D. P., et al. (2011), The ERA-Interim reanalysis: Configuration and performance of the data assimilation system, *Q. J. R. Meteorol. Soc.*, *137*(656), 553–597, doi:10.1002/qj.828.

Divine, D. V., and C. Dick (2006), Historical variability of sea ice edge position in the Nordic Seas, *J. Geophys. Res.*, *111*, C01001, doi:10.1029/2004JC002851.

Dunse, T., T. V. Schuler, J. O. Hagen, T. Eiken, O. Brandt, and K. A. Høgda (2009), Recent fluctuations in the extent of the firn area of Austfonna, Svalbard, inferred from GPR, *Ann. Glaciol.*, *50*(50), 155–162, doi:10.3189/172756409787769780.

Førland, E. J., and I. Hanssen-Bauer (2000), Increased precipitation in the Norwegian Arctic: True or false?, *Clim. Change*, *46*(4), 485–509, doi:10.1023/A:1005613304674.

Førland, E. J., R. Benestad, I. Hanssen-Bauer, J. E. Haugen, and T. E. Skaugen (2011), Temperature and precipitation development at Svalbard 1900–2100, *Adv. Meteorol.*, *2011*, 1–14, doi:10.1155/2011/893790.

Grabiec, M., J. Jania, D. Puczko, L. Kolondra, and T. Budzik (2012), Surface and bed morphology of Hansbreen, a tidewater glacier in Spitsbergen, *Polish Polar Res.*, *33*(2), 111–138, doi:10.2478/v10183-012-0010-7.

Hagen, J., K. Melvold, T. Eiken, E. Isaksson, and B. Lefauconnier (1999), Mass balance methods on Kongsvegen, Svalbard. Geografiska Annaler: Series A, *Phys. Geogr.*, *81*(4), 593–601, doi:10.1111/1468-0459.00087.

Hagen, J. O., J. Kohler, K. Melvold, and J.-G. Winther (2003a), Glaciers in Svalbard: Mass balance, runoff and freshwater flux, *Polar Res.*, *22*(2), 145–159, doi:10.1111/j.1751-8369.2003.tb00104.x.

Hagen, J. O., K. Melvold, F. Pinglot, and J. A. Dowdeswell (2003b), On the net mass balance of the glaciers and ice caps in Svalbard, Norwegian Arctic, *Arct. Antarct. Alp. Res.*, *35*(2), 264–270, doi:10.1657/1523-0430(2003)035[0264:OTNMBO]2.0.CO;2.

Hansen, B. B., R. Aanes, I. Herfindal, J. Kohler, and B.-E. Sæther (2011), Climate, icing, and wild arctic reindeer: Past relationships and future prospects, *Ecology*, *92*(10), 1917–1923, doi:10.1890/11-0095.1.

Hansen, B. B., K. Isaksen, R. E. Benestad, J. Kohler, Å. Ø. Pedersen, L. E. Loe, S. J. Coulson, J. O. Larsen, and Ø. Varpe (2014), Warmer and wetter winters: Characteristics and implications of an extreme weather event in the High Arctic, *Environ. Res. Lett.*, *9*(11), 114021, doi:10.1088/1748-9326/9/11/114021.

Hanssen-Bauer, I., and E. Førland (1998), Long-term trends in precipitation and temperature in the Norwegian Arctic: Can they be explained by changes in atmospheric circulation patterns?, *Clim. Res.*, *10*(1996), 143–153, doi:10.3354/cr010143.

Intergovernmental Panel on Climate Change (2013), *Climate Change 2013: The Physical Science Basis. Contribution of Working Group I to the Fifth Assessment Report of the Intergovernmental Panel on Climate Change*,T. F. Stocker et al., 1535 pp., Cambridge Univ. Press, Cambridge, U. K., and New York, doi:10.1017/CBO9781107415324.

Isaksson, E., et al. (2005), Two ice-cored δ18O records from Svalbard illustrating climate and sea-ice variability over the last 400 years, *Holocene*, *15*(4), 501–509, doi:10.1191/0959683605hl820rp.

Jaedicke, C., and P. Gauer (2005), The influence of drifting snow on the location of glaciers on western Spitsbergen, Svalbard, *Ann. Glaciol.*, *42*(1), 237–242, doi:10.3189/172756405781812628.

Karner, F., F. Obleitner, T. Krismer, J. Kohler, and W. Greuell (2013), A decade of energy and mass balance investigations on the glacier Kongsvegen, Svalbard, *J. Geophys. Res. Atmos.*, *118*, 3986–4000, doi:10.1029/2012JD018342.

Koch, S. E., M. DesJardins, and P. J. Kocin (1983), An interactive Barnes objective map analysis scheme for use with satellite and conventional data, *J. Clim. Appl. Meteorol.*, *22*(9), 1487–1503, doi:10.1175/1520-0450(1983)022<1487:AIBOMA>2.0.CO;2.

Kohler, J., and R. Aanes (2004), Effect of winter snow and ground-icing on a Svalbard reindeer population: Results of a simple snowpack model, *Arct. Antarct. Alp. Res.*, *36*(3), 333–341, doi:10.1657/1523-0430(2004)036[0333:EOWSAG]2.0.CO;2.

Kohler, J., T. D. James, T. Murray, C. Nuth, O. Brandt, N. E. Barrand, H. F. Aas, and A. Luckman (2007), Acceleration in thinning rate on western Svalbard glaciers, *Geophys. Res. Lett.*, *34*, L18502, doi:10.1029/2007GL030681.

König, M., J. Wadham, J.-G. Winther, J. Kohler, and A.-M. Nuttall (2002), Detection of superimposed ice on the glaciers Kongsvegen and midre Lovénbreen, Svalbard, using SAR satellite imagery, *Ann. Glaciol.*, *34*(1), 335–342, doi:10.3189/172756402781817617.

König, M., C. Nuth, J. Kohler, G. Moholdt, and R. Pettersen (2014), A digital glacier database for Svalbard, in *Global Land Ice Measurements from Space*, vol. 229–239, Springer, Berlin, doi:10.1007/978-3-540-79818-7.

Lang, C., X. Fettweis, and M. Erpicum (2015), Stable climate and surface mass balance in Svalbard over 1979–2013 despite the Arctic warming, *Cryosphere*, *9*(1), 83–101, doi:10.5194/tc-9-83-2015.

Liston, G. E., and K. Elder (2006a), A distributed snow-evolution modeling system (SnowModel), *J. Hydrometeorol.*, *7*(6), 1259–1276, doi:10.1175/JHM548.1.

Liston, G. E., and K. Elder (2006b), A meteorological distribution system for high-resolution terrestrial modeling (MicroMet), *J. Hydrometeorol.*, *7*(2), 217–234, doi:10.1175/JHM486.1.

Liston, G. E., and C. a. Hiemstra (2011), The changing cryosphere: Pan-Arctic snow trends (1979–2009), *J. Clim.*, *24*(21), 5691–5712, doi:10.1175/JCLI-D-11-00081.1.

Liston, G. E., and S. H. Mernild (2012), Greenland freshwater runoff. Part I: A runoff routing model for glaciated and nonglaciated landscapes (HydroFlow), *J. Clim.*, *25*(17), 5997–6014, doi:10.1175/JCLI-D-11-00591.1.

Liston, G. E., and M. Sturm (1998), A snow-transport model for complex terrain, *J. Glaciol.*, *44*(148), 498–516.

Liston, G. E., O. Bruland, H. Elvehøy, and K. Sand (1999), Below-surface ice melt on the coastal Antarctic ice sheet, *J. Glaciol.*, *45*(150), 273–285, doi:10.3189/002214399793377130.

Liston, G. E., R. B. Haehnel, M. Sturm, C. A. Hiemstra, S. Berezovskaya, and R. D. Tabler (2007), Instruments and methods simulating complex snow distributions in windy environments using SnowTran-3D, *J. Glaciol.*, *53*(181), 241–256, doi:10.3189/172756507782202865.

Martín-Español, A., F. Navarro, J. Otero, J. Lapazaran, and M. Błaszczyk (2015), Estimate of the total volume of Svalbard glaciers, and their potential contribution to sea-level rise, using new regionally based scaling relationships, *J. Glaciol.*, *61*(225), 29–41, doi:10.3189/2015JoG14J159.

Mernild, S. H., G. E. Liston, C. a. Hiemstra, and J. H. Christensen (2010), Greenland ice sheet surface mass-balance modeling in a 131-yr perspective, 1950–2080, *J. Hydrometeorol.*, *11*(1), 3–25, doi:10.1175/2009JHM1140.1.

Moholdt, G., J. O. Hagen, T. Eiken, and T. V. Schule (2010), Geometric changes and mass balance of the Austfonna ice cap, Svalbard, *Cryosphere*, *4*(1), 21–34, doi:10.5194/tcd-3-857-2009.

Möller, M., and C. Schneider (2015), Temporal constraints on future accumulation-area loss of a major Arctic ice cap due to climate change (Vestfonna, Svalbard), *Scientific Reports*, *5*, 8079, doi:10.1038/srep08079.

Möller, M., et al. (2011), Snowpack characteristics of Vestfonna and De Geerfonna (Nordaustlandet, Svalbard)—Spatiotemporal analysis based on multiyear snowpit data, *Geogr. Ann.*, *93*(4), 273–285, doi:10.1111/j.1468-0459.2011.00440.x.

Möller, M., F. Obleitner, C. H. Reijmer, V. A. Pohjola, P. Głowacki, and J. Kohler (2016), Adjustment of regional climate model output for modeling the climatic mass balance of all glaciers on Svalbard, *J. Geophys. Res. Atmos.*, *121*, 5411–5429, doi:10.1002/2015JD024380.

Nuth, C., T. V. Schuler, J. Kohler, B. Altena, and J. O. Hagen (2012), Estimating the long-term calving flux of Kronebreen, Svalbard, from geodetic elevation changes and mass-balance modelling, *J. Glaciol.*, *58*(207), 119–133, doi:10.3189/2012JoG11J036.

Oerlemans, J., and W. J. J. Van Pelt (2015), A model study of Abrahamsenbreen, a surging glacier in northern Spitsbergen, *Cryosphere*, *9*(2), 767–779, doi:10.5194/tc-9-767-2015.

Østby, T. I., T. V. Schuler, J. O. Hagen, R. Hock, and C. H. Reijmer (2013), Parameter uncertainty, refreezing and surface energy balance modelling at Austfonna ice cap, Svalbard, 2004–08, *Ann. Glaciol.*, *54*(63), 229–240, doi:10.3189/2013AoG63A280.

Pälli, A., J. C. Kohler, E. Isaksson, J. C. Moore, J. F. Pinglot, V. A. Pohjola, and H. Samuelsson (2002), Spatial and temporal variability of snow accumulation using ground-penetrating radar and ice cores on a Svalbard glacier, *J. Glaciol.*, *48*(162), 417–424.

Pohjola, V. A. A., T. A. Martma, H. A. J. Meijer, J. C. Moore, E. Isaksson, R. Vaikmae, and R. S. W. Van De Wal (2002), Reconstruction of three centuries of annual accumulation rates based on the record of stable isotopes of water from Lomonosovfonna, Svalbard, *Ann. Glaciol.*, *35*(1), 57–62, doi:10.3189/172756402781816753.

Reistad, M., Ø. Breivik, H. Haakenstad, O. J. Aarnes, and B. R. Furevik (2009), A high-resolution hindcast of wind and waves for the North Sea, the Norwegian Sea and the Barents Sea, Tech. Rep. Met.No Rep. No. 2009/14, Norwegian Meteorological Institute, Oslo.

Reistad, M., Ø. Breivik, H. Haakenstad, O. J. Aarnes, B. R. Furevik, and J.-R. Bidlot (2011), A high-resolution hindcast of wind and waves for the North Sea, the Norwegian Sea, and the Barents Sea, *J. Geophys. Res.*, *116*, C05019, doi:10.1029/2010JC006402.

Sauter, T., M. Möller, R. Finkelnburg, M. Grabiec, D. Scherer, and C. Schneider (2013), Snowdrift modelling for the Vestfonna ice cap, north-eastern Svalbard, *Cryosphere*, *7*(4), 1287–1301, doi:10.5194/tc-7-1287-2013.

Serreze, M. C., A. P. Barrett, J. C. Stroeve, D. N. Kindig, and M. M. Holland (2009), The emergence of surface-based Arctic amplification, *Cryosphere*, *3*(1), 11–19, doi:10.5194/tc-3-11-2009.

Serreze, M. C., A. D. Crawford, and A. P. Barrett (2015), Extreme daily precipitation events at Spitsbergen, an Arctic Island, *Int. J. Climatol.*, *35*(15), 4574–4588, doi:10.1002/joc.4308.

Taurisano, A., T. V. Schuler, J. O. Hagen, T. Eiken, E. Loe, K. Melvold, and J. Kohler (2007), The distribution of snow accumulation across the Austfonna ice cap, Svalbard: Direct measurements and modelling, *Polar Res.*, *26*(1), 7–13, doi:10.1111/j.1751-8369.2007.00004.x.

Undén, P., et al. (2002), HIRLAM-5 scientific documentation, Tech. Rep., Swedish Meteorological and Hydrological Institute, Norrköping, Sweden.

Uppala, S. M., et al. (2005), The ERA-40 re-analysis, *Q. J. R. Meteorol. Soc.*, *131*(612), 2961–3012, doi:10.1256/qj.04.176.

Van Pelt, W. J. J., and J. Kohler (2015), Modelling the long-term mass balance and firn evolution of glaciers around Kongsfjorden, Svalbard, *J. Glaciol.*, *61*(228), 731–744, doi:10.3189/2015JoG14J223.

Van Pelt, W. J. J., J. Oerlemans, C. H. Reijmer, V. A. Pohjola, R. Pettersson, and J. H. Van Angelen (2012), Simulating melt, runoff and refreezing on Nordenskiöldbreen, Svalbard, using a coupled snow and energy balance model, *Cryosphere*, *6*(3), 641–659, doi:10.5194/tc-6-641-2012.

Van Pelt, W. J. J., R. Pettersson, V. A. Pohjola, S. Marchenko, B. Claremar, and J. Oerlemans (2014), Inverse estimation of snow accumulation along a radar transect on Nordenskiöldbreen, Svalbard, *J. Geophys. Res. Earth Surf.*, *119*(4), 816–835, doi:10.1002/2013JF003040.

Winther, J.-G., O. Bruland, K. Sand, S. Gerland, D. Marechal, B. Ivanov, P. Głowacki, and M. König (2003), Snow research in Svalbard—An overview, *Polar Res.*, *22*(2), 125–144, doi:10.1111/j.1751-8369.2003.tb00103.x.

Zhang, X., J. He, J. Zhang, I. Polyakov, R. Gerdes, J. Inoue, and P. Wu (2012), Enhanced poleward moisture transport and amplified northern high-latitude wetting trend, *Nat. Clim. Change*, *3*(1), 47–51, doi:10.1038/nclimate1631.